

Enhanced nematicity emerging from higher-order van Hove singularities

Xinloong Han,^{1,*} Andreas P. Schnyder,^{2,†} and Xianxin Wu^{3,‡}

¹*Kavli Institute for Theoretical Sciences, University of Chinese Academy of Sciences, Beijing 100190, China*

²*Max-Planck-Institut für Festkörperforschung, Heisenbergstrasse 1, D-70569 Stuttgart, Germany*

³*CAS Key Laboratory of Theoretical Physics, Institute of Theoretical Physics,
Chinese Academy of Sciences, Beijing 100190, China*

(Dated: April 18, 2023)

Motivated by the experimental identification of a higher-order van Hove singularity (VHS) in AV_3Sb_5 kagome metals, we study electronic instabilities of 2D lattice models with higher-order VHS and flavor degeneracy. In contrast to conventional VHSs, the larger power-law density of states and the weaker nesting propensity of higher-order VHSs conspire together to generate distinct competing instabilities. After discussing the occurrence of higher-order VHSs on square and kagome lattice models, we perform unbiased renormalization group calculations to study competing instabilities and find a rich phase diagram containing ferromagnetism, anti-ferromagnetism, superconductivity and Pomeranchuk orders. Remarkably, there is a generic transition from superconductivity to a d -wave Pomeranchuk order with increasing flavor number. Implications for the intriguing quantum states of AV_3Sb_5 kagome metals are also discussed.

I. INTRODUCTION

Competing correlated electronic states are a central topic in condensed matter physics. A typical example is the close competition between spin density wave state and d -wave superconductivity near half filling in the Hubbard model on the square lattice^{1–4}. This could provide a possible explanation for the phase diagram of cuprate high- T_c superconductors. Importantly, band structures on the square lattice have a saddle point at which the Fermi surface topology changes from hole type to electron type. These saddle points are called van Hove singularity (VHS) points⁵ and display divergent density of states (DOS) in two dimension (2D). When the Fermi sea is filled up to the VHS, the Fermi surface takes the shape of a parallelogram and good Fermi surface nesting and the divergent DOS generate strong instabilities (double logarithmic) in both particle-particle and particle-hole channels. Similar physics also occur on the hexagonal lattices with repulsive interactions, where chiral ($d+id$)-wave superconductivity is found to be the ground state at van Hove filling in the formalism of renormalization group^{6–9}. Recently, another type of VHS, namely the higher-order VHS (HOVHS), was investigated in ABC-stacked trilayer graphene on hexagonal boron nitride¹⁰ and twisted bilayer graphene^{11–13}. It features flatter band dispersion along certain directions, while the Fermi surface touch tangentially at the saddle points¹². In the 2D case, the higher-order VHS exhibits power-law divergent DOS, much stronger than the logarithmic one of conventional VHS. Generally, such VHSs are characterized by relatively poor Fermi surface nesting when they are located at time-reversal invariant points. However, the strongly divergent DOS can promote exotic correlated phenomena such as ferromagnetism and supermetal^{12,14,15}.

The corresponding quantum materials convey VHSs play an essential role in revealing the origin of correlated electronic states. Despite tremendous experimental efforts, superconductivity has not been achieved in

graphene near VHS filling possibly due to disorder effect. Recently, the new family of kagome metals AV_3Sb_5 ($A=\text{K}, \text{Rb}, \text{Cs}$) with V kagome nets^{16–19} has been discovered, which exhibits a higher-order VHS and several conventional VHSs close to the Fermi level. The higher-order VHS is located just below the Fermi level and exhibits a flat dispersion along the M-K direction with a dominant quartic term, as confirmed by ARPES experiments^{20,21}. This multitude of VHSs may be closely related to a number of exotic correlated phenomena that occur in AV_3Sb_5 , such as charge density wave (CDW)^{22–31}, unconventional superconductivity^{32–35}, and nematic orders^{34,36–39}. The unconventional nature of superconductivity in AV_3Sb_5 is evidenced by a large residual thermal conductivity³², and proximity-induced edge supercurrents³³ and double superconducting domes under pressure^{40–42}. Below the transition temperature $T_{\text{CDW}} = 78 - 103\text{K}$ ^{22–24,27} AV_3Sb_5 exhibits an unconventional CDW order with a 2×2 in-plane pattern and time-reversal symmetry breaking, while below $T_{\text{nem}} = 35\text{K}$ a nematic order emerges^{34,36–39}. There also exist the sublattice features in the kagome metal which relates to the "sublattice interference effect"⁴³ due to the completely different wave function support with filling. Two-fold VHS which have two opposite concavity originated from a pure and a mixed sublattice states near Fermi level, has suggested to have a competition between chiral excitonic state and CDW order⁴⁴. Recently, a renormalization group study⁴⁵ also explored this sublattice feature and showed its important influence on the ordering tendencies.

Higher-order VHSs have also been observed in other materials, such as $\text{Sr}_3\text{Ru}_2\text{O}_7$ ⁴⁶, $\beta\text{-YbAlB}_4$ ⁴⁷ and germanene on MoS_2 ⁴⁸. In addition, twisted bilayer graphene and multi-orbital systems can host VHSs with multiple fermion flavours N_f originating either from valley or orbital degrees of freedom. The increased flavor number can have a significant effect on instabilities, for example, an imaginary CDW order instead of chiral superconductivity is favored on the hexagonal lattices with conven-

tional VHSs for $N_f \geq 4$ ⁴⁹.

Motivated by the above observations, we systematically study the competing instabilities on the 2D square and hexagonal lattices at higher-order van Hove filling with an $SU(N_f)$ flavor degeneracy and focus on the effect of the number of flavors. First, based on tight-binding models, we determine the conditions for the occurrence of higher-order VHSs on the square and kagome lattices. With this information we derive general effective models describing the N_p higher-order van Hove saddle points with N_f fermion flavors. Based upon the low-energy models we perform unbiased renormalization group calculations to deduce the competing instabilities. Remarkably, we find that increasing flavor number can drive a generic phase transition from a superconducting order to a nematic order. Finally, we perform mean-field analyses to determine the ground states and discuss the competing orders in the kagome lattice model. Implications for the the AV_3Sb_5 kagome metals are also discussed.

II. HIGHER-ORDER VHS ON THE SQUARE AND KAGOME LATTICES

In this section, we derive the conditions for the occurrence of higher-order VHSs in tight-binding models on the square and kagome lattices. This provides a starting point for the renormalization group study in the next section.

A. Square lattice

We start by discussing VHSs in the square lattice with the dispersion

$$\epsilon_{\mathbf{k}} = -2t(\cos k_x + \cos k_y) - 4t' \cos k_x \cos k_y - 2t''(\cos 2k_x + \cos 2k_y) - \mu, \quad (1)$$

where t , t' and t'' are the nearest-neighbor (NN), second NN and third NN hopping amplitudes, respectively. Near the saddle point at $X = (\pi, 0)$, the effective dispersion is

$$\begin{aligned} \epsilon_X(\mathbf{k}) = & (-t - 2t' + 4t'')k_x^2 + (t - 2t' + 4t'')k_y^2 \\ & + \frac{t + 2t' - 16t''}{12}k_x^4 + \frac{-t + 2t' - 16t''}{12}k_y^4 \\ & + t'k_x^2k_y^2 + 4(t' - t'') - \mu. \end{aligned} \quad (2)$$

where $k_{x,y}$ are the momentum relative to the X point. The effective dispersion around the other saddle point $Y = (0, \pi)$ can be obtained by a four-fold rotation and is $\epsilon_Y(\mathbf{k}) = \epsilon_X(k_y, -k_x)$. With only NN hopping, $\epsilon_X(\mathbf{k}) = -t(k_x^2 - k_y^2)$ and there are two conventional VHS points at X and Y. When one coefficient of the quadratic terms vanishes in Eq. (2), a conventional VHS point transforms into an higher-order VHS point, i.e. $t''_c = -(\pm t - 2t')/4$ with $t' \neq 0$. In this case, the dispersion along k_x or k_y become quartic and exhibit a nearly flat dispersion near the VHS point. Fig. 1 (a) shows the band evolution

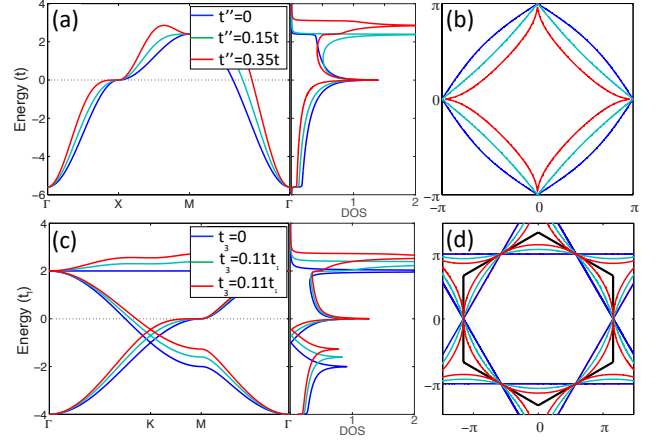


FIG. 1. Band dispersion, density of states (DOS) and Fermi surfaces with variation of hopping parameters for the square lattice (top) and kagome lattice (bottom). A fixed $t' = 0.2t$ is adopted with $\mu = 4(t' - t'')$ for the square lattice model, while for the kagome lattice model we set $t_2 = 0$ and $\mu = 2t_3$.

with a variation of t'' for $t' = 0.2t$ and $\mu = 4(t' - t'')$. It is apparent that the dispersion along k_x near the X point becomes flatter with increasing t'' . The corresponding evolution of the Fermi surface at the van Hove filling is displayed in Fig. 1 (b). At the critical parameter $t''_c = 0.35t$, the Fermi surface becomes circular-like centered at (π, π) and touches tangentially at X and Y points, which is a typical character of higher-order VHS. In the square lattice, there are two higher-order VHSs.

B. Kagome lattice

Next, we study the VHSs in kagome lattice models by use of the tight-binding Hamiltonian,

$$\begin{aligned} \mathcal{H}_0 = & [t_1 \sum_{\langle ij \rangle \sigma} c_{i\sigma}^\dagger c_{j\sigma} + t_2 \sum_{\langle\langle ij \rangle\rangle \sigma} c_{i\sigma}^\dagger c_{j\sigma} + t_3 \sum_{\langle\langle\langle ij \rangle\rangle\rangle \sigma} c_{i\sigma}^\dagger c_{j\sigma} \\ & + h.c.] - \mu \sum_{i\sigma} c_{i\sigma}^\dagger c_{i\sigma}, \end{aligned} \quad (3)$$

where t_1 , t_2 and t_3 denotes the NN, second NN and third NN hopping amplitudes, respectively. In momentum space, the Hamiltonian can be written as $\mathcal{H}_0 = \sum_{\mathbf{k}\sigma} \psi_{\mathbf{k}\sigma}^\dagger (h(\mathbf{k}) - \mu) \psi_{\mathbf{k}\sigma}$ with $\psi_{\mathbf{k}\sigma}^\dagger = [c_{A\sigma}^\dagger(\mathbf{k}), c_{B\sigma}^\dagger(\mathbf{k}), c_{C\sigma}^\dagger(\mathbf{k})]$ and A, B, C being the three sub-lattice indices. The Hamiltonian matrix elements are,

$$\begin{aligned} h_{11} &= 2t_3 \cos k_y, \\ h_{22/33} &= 2t_3 \cos\left(\frac{\sqrt{3}}{2}k_x \pm \frac{1}{2}k_y\right), \\ h_{12/13} &= 2t_1 \cos\left(\frac{\sqrt{3}}{4}k_x \mp \frac{1}{4}k_y\right) + 2t_2 \cos\left(\frac{\sqrt{3}}{4}k_x \pm \frac{3}{4}k_y\right), \\ h_{23} &= 2t_1 \cos \frac{1}{2}k_y + 2t_2 \cos \frac{\sqrt{3}}{2}k_x, \end{aligned} \quad (4)$$

with $h_{\beta\alpha} = h_{\alpha\beta}^*$ for $\alpha \neq \beta$. The band dispersion features a flat band and two Dirac cones. Moreover, there are two types of VHSs located at $E = 2t_3$ and $E = 2(t_1 - t_2 - t_3)$, featuring pure sublattice (p-type) or mixed sublattice (m-type) characters, respectively³⁵. In order to explore

the realization of higher-order VHSs on kagome lattice models, we derive a low-energy effective model near the saddle points. The effective Hamiltonian around the $M_1 = (\frac{2\pi}{\sqrt{3}}, 0)$ point reads,

$$h_{M_1}(\mathbf{q}) = \begin{pmatrix} 2t_3(1 - \frac{1}{2}q_y^2) & cq_x + dq_y & cq_x - dq_y \\ cq_x + dq_y & -2t_3[1 - \frac{1}{2}(\frac{\sqrt{3}}{2}q_x + \frac{1}{2}q_y)^2] & 2(t_1 - t_2) - \frac{t_1}{4}q_y^2 + \frac{3t_2}{4}q_x^2 \\ cq_x - dq_y & 2(t_1 - t_2) - \frac{t_1}{4}q_y^2 + \frac{3t_2}{4}q_x^2 & -2t_3[1 - \frac{1}{2}(\frac{\sqrt{3}}{2}q_x - \frac{1}{2}q_y)^2] \end{pmatrix},$$

where $c = -\sqrt{3}(t_1 + t_2)/2$, $d = (t_1 - 3t_2)/2$ and $\mathbf{q} = (q_x, q_y)$ is the momenta relative to the M_1 point. For the p-type VHS with $E = 2t_3$, the energy dispersion up to the quadratic order is,

$$E_p^{M_1}(\mathbf{q}) = 2t_3 - \frac{3(t_1 + t_2)^2}{4(t_1 - t_2 - 2t_3)}q_x^2 + \left[\frac{(t_1 - 3t_2)^2}{4(t_1 - t_2 + 2t_3)} - t_3 \right]q_y^2. \quad (5)$$

The effective dispersion around $M_2 = (\frac{\pi}{\sqrt{3}}, \pi)$ and $M_3 = (-\frac{\pi}{\sqrt{3}}, \pi)$ can be obtained by six-fold rotations, namely $E_p^{M_2}(\mathbf{q}) = E_p^{M_1}(\hat{C}_6\mathbf{q})$ and $E_p^{M_3}(\mathbf{q}) = E_p^{M_1}(\hat{C}_3\mathbf{q})$. With only nearest-neighbor hopping, i.e. $t_2 = t_3 = 0$, this VHS is conventional and features perfect Fermi surface nesting with $E_p^{M_1} = 2t_3 - \frac{t_1}{4}(3q_x^2 - q_y^2)$. In order to realize a higher-order VHS, that is, one of two quadratic terms in Eq. (5) must vanish. As the quadratic and quartic terms of q_x vanish simultaneously with $t_1 = -t_2$, we consider the q_y terms. Setting the coefficient of q_y^2 to zero, we obtain $t_{3c} = \frac{1}{4}(-t_1 + t_2 \pm \sqrt{3t_1^2 - 14t_2t_1 + 19t_2^2})$. The corresponding evolution of band structures and Fermi surfaces at the VHS filling is displayed in Fig. 1 (c) and (d). At the critical parameter t_{3c} , the band dispersion along M-K is quartic and the corresponding Fermi surfaces are circular-like around the center. In particular, for $t_3 = 0$, the coefficients for q_y^2 and q_y^4 will vanish simultaneously, generating a higher-order VHS with more strongly divergent DOS. The DOS for a generalized dispersion $\epsilon(\mathbf{q}) = aq_x^2 - bq_y^{2\alpha'} + \dots$ ($\alpha' > 1$) is^{12,14},

$$\rho(\epsilon) = \begin{cases} \rho_+ \epsilon^{-\kappa}, & \text{for } \epsilon > 0 \\ \rho_- \epsilon^{-\kappa}, & \text{for } \epsilon < 0 \end{cases} \quad (6)$$

where $\kappa = 1/2 - 1/(2\alpha')$, $\rho_+ = \Gamma[1/(2\alpha')]\Gamma[1/2 - 1/(2\alpha')]/(4\alpha'\pi^{5/2}a^{1/2}b^{1/2\alpha'})$ and $\rho_- = \rho_+ \sin[\pi/(2\alpha')]$. The DOS is asymmetrical with respect to zero, as shown in Fig. 1 (a) and (c) from numerical calculations. When only the quadratic term vanishes, $\alpha' = 2$ and $\kappa = 1/4$. While both quadratic and quartic terms vanish, $\alpha' = 3$ and $\kappa = 1/3$.

For the m-type VHS with $E = 2(t_1 - t_2 - t_3)$, the

energy dispersion up to the second order at M_1 point is,

$$E_m^{M_1}(\mathbf{q}) = 2(t_1 - t_2 - t_3) + \frac{3(t_1 - t_3)(t_1 + 3t_2 + 2t_3)}{4(t_1 - t_2 - 2t_3)}q_x^2 + \frac{1}{4}(t_3 - t_1)q_y^2. \quad (7)$$

Within this model, the vanishing of the quadratic term will lead to a completely flat dispersion along the corresponding direction. A higher-order VHS can be realized upon the inclusion of longer-range hopping. On the kagome lattice, there are three inequivalent M points thus three saddle points.

III. THE GENERAL MODEL

We further investigate the competing instabilities at the higher-order van Hove filling. Since the unbiased RG method takes into account the particle-particle and particle-hole channels on equal footing, and the low-energy physics is dominated by the electron scattering in the vicinity of saddle points, we simplify the above models into patch models, which only consider the electrons near the saddle points^{3,6,50}, and then perform a RG analysis. The general low-energy theory with total N_p patches and N_f flavors of fermions with the $SU(N_f)$ symmetry is given by^{6,14},

$$\begin{aligned} \mathcal{L} = & \sum_{\alpha\sigma} \psi_{\alpha\sigma}^\dagger (\partial_\tau - \epsilon_{\alpha,\mathbf{k}} + \mu) \psi_{\alpha\sigma} + \sum_{\sigma\sigma'} \left\{ \sum_{\alpha} g_4 \psi_{\alpha\sigma}^\dagger \psi_{\alpha\sigma'}^\dagger \right. \\ & \times \psi_{\alpha\sigma'} \psi_{\alpha\sigma} + \sum_{\alpha \neq \alpha'} [g_1 \psi_{\alpha\sigma}^\dagger \psi_{\alpha'\sigma'}^\dagger \psi_{\alpha\sigma'} \psi_{\alpha'\sigma} + g_2 \psi_{\alpha\sigma}^\dagger \\ & \times \psi_{\alpha'\sigma'}^\dagger \psi_{\alpha'\sigma'} \psi_{\alpha\sigma} + g_3 \psi_{\alpha\sigma}^\dagger \psi_{\alpha\sigma'}^\dagger \psi_{\alpha'\sigma'} \psi_{\alpha'\sigma}] \left. \right\}, \end{aligned} \quad (8)$$

where the patch index $\alpha, \alpha' = 1, \dots, N_p$, and the spin/flavor index $\sigma, \sigma' = 1, \dots, N_f$. $\psi_{\alpha\sigma}$ ($\psi_{\alpha\sigma}^\dagger$) are electron annihilation (creation) operators with spin/flavor σ at patch α . Here $\epsilon_{\alpha,\mathbf{k}}$ is the energy dispersion of electrons expanded up to $2n$ -th order at patch α , where n is a positive integer ($n = 1$ for conventional VHS). The chemical potential is denoted by μ . In the rest of the paper, we take $\mu = 0$ and $n = 2$. The short-range interactions

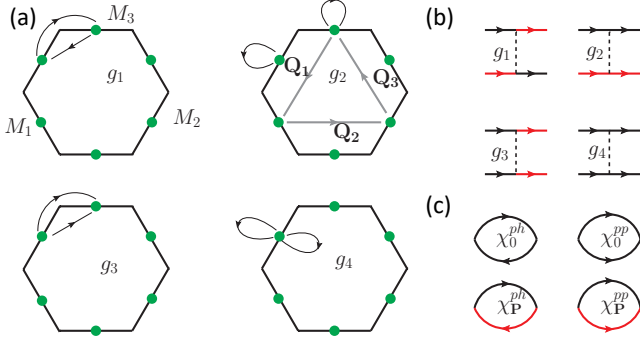


FIG. 2. (a) Four different scattering processes in the kagome lattice with three different patches. Here $\mathbf{Q}_1, \mathbf{Q}_2$ and \mathbf{Q}_3 represent the nesting vectors between two patches. (b) Feynman diagrams describing these four scattering processes. The lines with different colors represent fermions in different patches. (c) Feynman diagrams representing the particle-hole and particle-particle polarizations with zero or finite momentum transfer $\mathbf{P} = \mathbf{Q}_{1,2,3}$ at the zero order.

g_i which describe different scattering processes are illustrated in the Fig. 2. One should note the Umklapp scattering g_4 appear when the nesting momentum $2\mathbf{Q} = 0$ up to a reciprocal lattice vectors. The inclusion of only short-range interactions in the low-energy description is justified because the highly metallic screening close to VHSs suppresses long-ranged Coulomb interactions.

The higher-order VHSs possess distinct properties compared with conventional VHSs. First, the corresponding DOS at a given patch diverges with a power law, i.e., faster than the logarithmic divergence at a conventional VHS. And second, the nesting between different patches is weaker compared to the case with conventional VHSs. These two physical properties can be checked from the zero momentum and finite momentum (difference between distinct patches) susceptibilities. The zero momentum particle-particle and particle-hole susceptibilities can be defined as $\chi_0^{ph}(\Lambda/T) = -T \sum_{i\omega_m} \int \frac{d^2\mathbf{k}}{(2\pi)^2} G_\alpha^0(i\omega_m, \mathbf{k}) G_\alpha^0(i\omega_m, \mathbf{k})$ and $\chi_0^{pp}(\Lambda/T) = T \sum_{i\omega_m} \int \frac{d^2\mathbf{k}}{(2\pi)^2} G_\alpha^0(-i\omega_m, -\mathbf{k}) G_\alpha^0(i\omega_m, \mathbf{k})$, respectively. Note we have hid the patch index α in susceptibility $\chi_0^{ph,pp}$ because of the lattice symmetry. Here $G_\alpha^0(i\omega_m, \mathbf{k}) = 1/(i\omega_m - \xi_{\alpha,\mathbf{k}})$ is the bare Green's function of electrons at patch α with $\xi_{\alpha,\mathbf{k}} = \epsilon_{\alpha,\mathbf{k}} - \mu$. T is the temperature of the system, and the magnitude of momentum has an ultraviolet cutoff Λ . Matsubara-frequency for the electrons is taken as $i\omega_m = i(2m+1)T$ with $m = 0, \pm 1, \pm 2, \dots$. Focusing on the van Hove filling with $\mu = 0$, we find that susceptibilities with zero momentum transfer exhibit the same power-law divergent behavior but with different prefactors, i.e., with $\chi_0^{pp}, \chi_0^{ph} \propto (\rho_+ + \rho_-)/(2T^\kappa)$. While the finite momentum susceptibilities $\chi_{\mathbf{P}_{\alpha\beta}}^{ph}(\Lambda/T) = -T \sum_{i\omega_m} \int \frac{d^2\mathbf{k}}{(2\pi)^2} G_\alpha^0(i\omega_m, \mathbf{k}) G_\beta^0(i\omega_m, \mathbf{P}_{\alpha\beta} + \mathbf{k})$ +

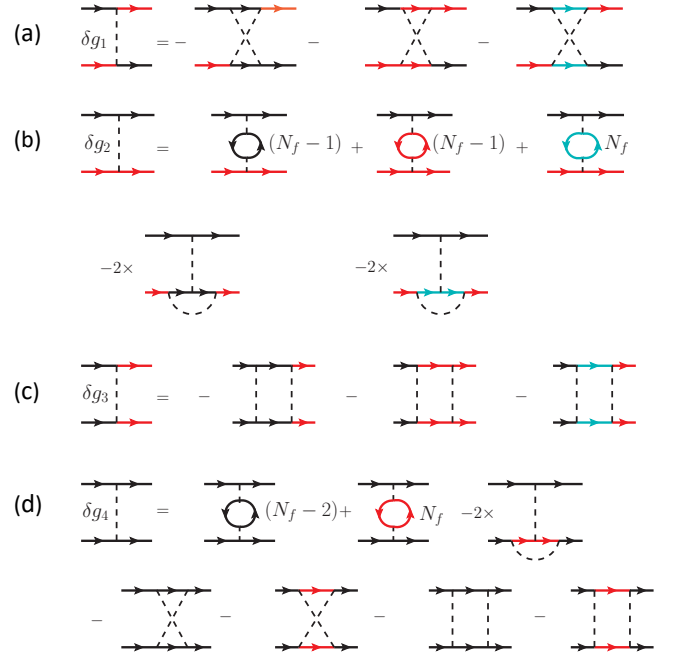


FIG. 3. Feynman diagrams for the one-loop corrections of the four different scattering processes g_i with the inclusion of dominant susceptibilities. The lines with different colors denote the different patches. (a) To the leading order, only the crossed diagrams contribute to the backward scattering process between two patches. (b) Two different topological Feynman diagrams contribute to the renormalization of the inter-patch forward scattering process g_2 between two different patches. (c) There are three BCS type diagrams to correct the umklapp scattering g_3 . (d) The diagrams to renormalize the intra-patch forward scattering g_4 .

$\mathbf{k})$ and $\chi_{\mathbf{P}_{\alpha\beta}}^{pp}(\Lambda/T) = T \sum_{i\omega_m} \int \frac{d^2\mathbf{k}}{(2\pi)^2} G_\alpha^0(-i\omega_m, -\mathbf{k}) G_\beta^0(i\omega_m, \mathbf{P}_{\alpha\beta} + \mathbf{k})$ where patches $\alpha \neq \beta$ and finite momentum $\mathbf{P}_{\alpha\beta} = \mathbf{Q}_{1,2,3}$ as shown in Fig. 2 (a), exhibit quite different behavior, $\chi_{\mathbf{P}_{\alpha\beta}}^{ph} \propto \text{const}$, and $\chi_{\mathbf{P}_{\alpha\beta}}^{pp} \propto \ln(\Lambda/T)$ ¹⁴. Therefore, approaching zero temperature, the zero momentum susceptibility $\chi_0^{pp/ph}$ diverges much faster than the ones with finite momentum $\chi_{\mathbf{P}}^{pp/ph}$, in contrast to conventional VHSs. These characteristics play an essential role in determining the competing orders. Note we have hid the patch index α in susceptibility $\chi_0^{ph,pp}$ because of the lattice symmetry.

IV. RG FLOW EQUATIONS

After presenting the effective model and analysis of susceptibilities, we turn to study the competing instabilities by performing renormalization group calculations. Within the renormalization group (RG) approach, high-energy degrees of freedom are iteratively integrated out, such that the initial microscopic description gradually

evolves to an effective low-energy model with decreasing energy cutoff. The initial microscopic description and the effective low-energy model have the same form, except for the coupling constants which depend on a running parameter, i.e., the RG flow time. The coupling constants can grow or shrink under the RG flow, which are relevant and irrelevant couplings, respectively. Approaching a critical RG time, one or several coupling constants can diverge and the system goes to a strong-coupling regime. Usually the susceptibility of certain order will also diverge, indicating that the system undergoes a phase transition to an ordered state. In fermionic systems interactions with finite frequency and/or momentum away from the Fermi surface are irrelevant, such that only zero-frequency coupling constants at the Fermi surface need to be considered^{51,52}.

For these higher-order VHSs, the corrections of the coupling constants from both tree-level and one-loop terms are important and dimensionless coupling constants $\tilde{g}_i = g_i \partial \chi_0^{pp} / \partial s$ can be introduced with $s = \ln(\Lambda/T)$. Generally, there are no stable fixed points and thus we focus on the strong-coupling behavior of the dimensional couplings g_i ^{14,15}, where the tree-level terms are irrelevant. The RG flow equations with the one-loop terms can be obtained directly by implementing the Feynman diagrams as shown in Fig. 2 with the inclusion of dominant susceptibilities in the particle-particle and particle-hole channels. Here, we derive general RG flow equations for N_p patches and N_f flavors, such that different lattice structures and different numbers of orbital and spin degeneracies can be captured. The same result is also derived in Ref.¹⁴. As depicted by Fig. 2, the fermions in different patches are denoted by different colors, then we have to sum over the remaining fermion patch numbers. Since there is no flavor flip process, the summation over the fermion flavor only occur in the fermion loop. To simplify the identification of the critical temperature, we adopt $y = \chi_0^{pp}(T) - \chi_0^{pp}(\Lambda) = \rho_0 f(\kappa) \Lambda^{-\kappa} ((\Lambda/T)^\kappa - 1)$ as the RG flow time, with $\rho_0 = (\rho_+ \rho_-)/2$ and $f(\kappa) = \frac{1}{2} \int d\epsilon |\epsilon|^{-(1+\kappa)} \tanh(\epsilon/2)$ ¹⁴. Straightforwardly, we obtain the RG flow equations after considering the one-loop corrections in Fig. 3,

$$\frac{dg_1}{dy} = d_0 g_1 [2g_4 + (N_p - 2)g_1], \quad (9)$$

$$\begin{aligned} \frac{dg_2}{dy} = & -d_0 (N_p - 2)g_2 [N_f g_2 - 2g_1] \\ & - 2d_0 g_4 [(N_f - 1)g_2 - g_1], \end{aligned} \quad (10)$$

$$\frac{dg_3}{dy} = -g_3 [(N_p - 2)g_3 + 2g_4], \quad (11)$$

$$\begin{aligned} \frac{dg_4}{dy} = & -d_0 \left\{ (N_p - 1) [N_f g_2^2 - 2g_1 g_2 - g_1^2] \right. \\ & \left. + (N_f - 3)g_4^2 \right\} - g_4^2 - (N_p - 1)g_3^2. \end{aligned} \quad (12)$$

Here, the nesting parameter $d_0 = \partial \chi_0^{ph} / \partial \chi_0^{pp}$. It is noted that we have ignored subdominant terms related to susceptibilities with large momentum transfer, as they have

weaker divergence than $\chi_0^{pp/ph}$. The RG equations have two prominent features: (1) the RG equations for g_1 and g_3 contain g_1 and g_3 , respectively; (2) the RG functions for g_1 and g_2 do not contain g_3 and that of g_3 does not contain g_1 and g_2 , in contrast to the RG equations of conventional VHSs⁶. The first feature is related to a symmetry: all interactions except g_1 conserve spin at each saddle point separately and all interaction except g_3 conserve the number of electrons at each saddle point separately. Consequently, the RG equation of a nonconserving interactions $g_{1,3}$ must contain a factor of itself, indicating that the sign of g_1 and g_3 will be fixed during the RG flow. The second feature is related to the neglect of subdominant terms and suggests that g_1 and g_2 are fully decoupled with g_3 during the RG evolution.

The magnitude of d_0 dramatically affects the flow of the RG, determining which coupling constant will diverge first. One can check this by considering the limit of small $d_0 \rightarrow 0$ and the limit of large $d_0 \rightarrow \infty$, respectively. When $d_0 = 0$, the coupling constants g_1 and g_2 will not flow, staying at the given initial values for the RG time y running from the ultraviolet (UV) value to the infrared (IR) value. The negative definite character of the differential equation Eq. (12) for g_4 at $d_0 = 0$ will ensure that the coupling constant g_4 always flows to negative infinity, except for the trivial fixed point $(g_3, g_4) = (0, 0)$. Thus, in the limit of small d_0 superconducting order is favored, while the instability in the particle-hole channel, such as charge-density wave (CDW), ferromagnetic (FM) and anti-ferromagnetic (AFM) order, is completely suppressed. In contrast, in the large d_0 limit the particle-hole instabilities are favored, while the particle-particle channel leading to superconductivity is suppressed. The coupling constant g_i that diverges first at the RG time y_c determines the leading order and the corresponding transition temperature is $T_c \propto (\rho_0 f(\kappa) / (\rho_0 f(\kappa) + \Lambda^\kappa y_c))^{1/\kappa}$. We note that this power-law behavior of T_c in systems with HOVHs is significantly different from the exponential behavior of T_c in systems with conventional VHSs^{3,6}.

V. ORDERING INSTABILITIES

To identify the leading instabilities, we introduce the test vertices in various particle-particle and particle-hole channels, $\delta \mathcal{L} = \sum [\Delta \psi^\dagger \psi^{(\dagger)} + h.c.]$. In the particle-particle channel, we consider the flavor pairing $\Delta_\alpha [\psi_{\alpha\sigma}^\dagger \psi_{\alpha\sigma'}^\dagger - \psi_{\alpha\sigma'}^\dagger \psi_{\alpha\sigma}^\dagger]$ with $\sigma > \sigma'$ and it is antisymmetric in the flavor space. In the particle-hole channel, the charge Pomeranchuk order is the summation of uniform flavor terms $\sum_\sigma \psi_{\alpha\sigma}^\dagger \psi_{\alpha\sigma}$ and the magnetic order is the summation of the antisymmetric terms $\sum_{\sigma > \sigma'} [\psi_{\alpha\sigma}^\dagger \psi_{\alpha\sigma'} - \psi_{\alpha\sigma'}^\dagger \psi_{\alpha\sigma}]$. Under the RG flow, these test vertices obtain one-loop corrections through the divergent susceptibilities and the corresponding RG equa-

TABLE I. Competing orders and their divergent coefficients λ_I . The orders in three channels can be s -wave and d -wave depending on their symmetry and they are labelled as sCO or sCO with CO=POM, FM SC. In the square lattice, these orders are singlet, while in the hexagonal lattice, the d -wave orders are doublets.

Competing order	coefficient λ_I
sPOM	$d_0(N_p - 1)(G_1 - N_f G_2) - d_0(N_f - 1)G_4$
dPOM	$d_0(-G_1 + N_f G_2) - d_0(N_f - 1)G_4$
FM	$d_0(N_p - 1)G_1 + d_0 G_4$
dFM	$-d_0 G_1 + d_0 G_4$
sSC	$-(N_p - 1)G_3 - G_4$
dSC	$G_3 - G_4$

tion reads,

$$\frac{d\Delta_\alpha(y)}{dy} = V_{\alpha\beta}(y)\Delta_\beta(y). \quad (13)$$

These orders can be further decoupled into different irreducible channels according to the lattice symmetry, $\dot{\Delta}^I(y) = V_{\Delta^I}(y)\Delta^I(y)$ where $V_{\Delta^I}(y)$ is the interaction vertex for Δ^I and is a linear combination of coupling constants. Approaching the critical RG time, the interaction g_i usually diverges as $g_i(y) = G_i/(y_c - y)$, hence $V_{\Delta^I}(y)$ diverges as $V_{\Delta^I}(y) = \lambda_I/(y_c - y)$ where λ_I is a constant number. Correspondingly, the vertex scales as $\Delta^I(y) \propto (y_c - y)^{-\lambda_I}$ and the susceptibility χ_I related to Δ^I scales as $\chi_I(y) \propto (y_c - y)^{-\eta_I}$ with $\eta_I = 2\lambda_I - 1$ from the equation $d\chi_I/dy \propto |\Delta^I|^2$. The parameters for two representative orders are $\lambda_{dSC} = G_3 - G_4$ for the d -wave pairing and $\lambda_{dPOM} = -d_0 G_1 + d_0 N_f G_2 - d_0(N_f - 1)G_4$ for the d -wave Pomeranchuk order. The order with the most positive λ_I diverges fastest and is the leading instability. We summarize the interactions and their coefficients for various competing orders in particle-particle and particle-hole channels in the Table. I.

VI. FIXED TRAJECTORIES AND STABILITIES

In the RG equations (9)-(12) for the higher-order VHSs, there is no positive definite coupling constant, distinct from the case of conventional VHS⁶. The RG flow of differential equations (9)-(12) exhibit fixed trajectories along which the couplings become singular but their ratios tend to finite values. Along these fixed trajectories the couplings g_i diverge as $g_i(y) = \frac{G_i}{y_c - y}$, as mentioned before. To analyze the stability of these fixed trajectories, it is useful to introduce the relative couplings $\gamma_i = g_i/g_4$ with $i = 1, 2, 3$. The reason that we choose g_4 as the denominator is that the g_4 always diverges except for the trivial unstable initial condition $g_i(0) = 0$. This means that $|g_4|$ monotonically grows near critical RG time y_c . Thus we choose $x = \ln|g_4(y)|$ as a running parameter and the reduced RG equations for γ_i ($i = 1, 2, 3$) for given $N_p = 2$ as a typical example are given by

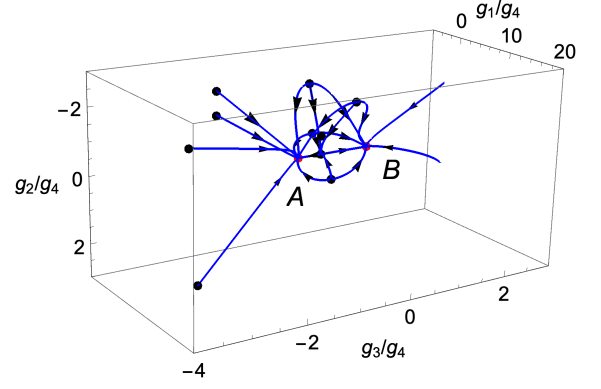


FIG. 4. 3D RG flow diagram of $(\frac{g_1}{g_4}, \frac{g_2}{g_4}, \frac{g_3}{g_4})$ under RG time y with a given initial $g_4(y=0) = -0.1$, number of fermion flavors $N_f = 4$ and patches $N_p = 3$, and the nesting parameter $d_0 = 0.1$. Here the black points denote the unstable fixed points for the reduced RG equations, and they eventually flow to the stable points indicated by red points, which are labeled as A and B, respectively.

$$\beta_1(\{\gamma_i\}) = \frac{d\gamma_1}{dx} = \frac{2d_0\gamma_1}{f(\gamma_1, \gamma_2, \gamma_3)} - \gamma_1, \quad (14)$$

$$\beta_2(\{\gamma_i\}) = \frac{d\gamma_2}{dx} = \frac{-2d_0[(N_f - 1)\gamma_2 - \gamma_1]}{f(\gamma_1, \gamma_2, \gamma_3)} - \gamma_2, \quad (15)$$

$$\beta_3(\{\gamma_i\}) = \frac{d\gamma_3}{dx} = \frac{-2\gamma_3}{f(\gamma_1, \gamma_2, \gamma_3)} - \gamma_3, \quad (16)$$

where $f(\gamma_1, \gamma_2, \gamma_3) = -d_0 N_f \gamma_2^2 + 2d_0 \gamma_1 \gamma_2 + d_0 \gamma_1^2 - \gamma_3^2 - d_0(N_f - 1) - 1$. Since in this system G_4 is always non vanishing (we ignore the trivial solution $G_4 = 0$), then the fixed points for the reduced RG equations are $(\Gamma_i = G_i/G_4)$. The reason we analyze the reduced RG equations (14-16) is that determining the stability conditions of the fixed trajectories in RG equations (9-12) can be obtained by studying the stability condition of its corresponding fixed points in reduced RG equations. The matrix $S_{ij} = (\partial\beta_i/\partial\gamma_j)|_{(\Gamma_i)}$ is so-called stability matrix⁵³ and the signs of its eigenvalues determine the stability of the fixed point $(\Gamma_1, \Gamma_2, \Gamma_3)$. If all eigenvalues of the matrix \mathbf{S} at the fixed point (Γ_i) are non-positive, then the fixed point $(\Gamma_i = G_i/G_4)$ or the corresponding trajectory (G_1, G_2, G_3, G_4) is immune to perturbation around the fixed point, in other words, it is a stable solution. For the square lattice with $N_p = 2$ patches and general flavor number N_f , the analysis of the stability of fixed points is straightforward and we give all fixed points, their stable conditions and corresponding dominant orders in the Appendix A. We find that instabilities in both particle-particle and particle-hole channels can be leading but a large N_f favors particle-hole orders. For the hexagonal lattice with $N_p = 3$, we can obtain all fixed trajectories provided in the Appendix B but the analysis for conditions of stability and competing orders need numerical calculations. For the more general case with fermion patches N_p and flavors N_f , the analytical trajectories are difficult to obtain but one can identify the fixed points

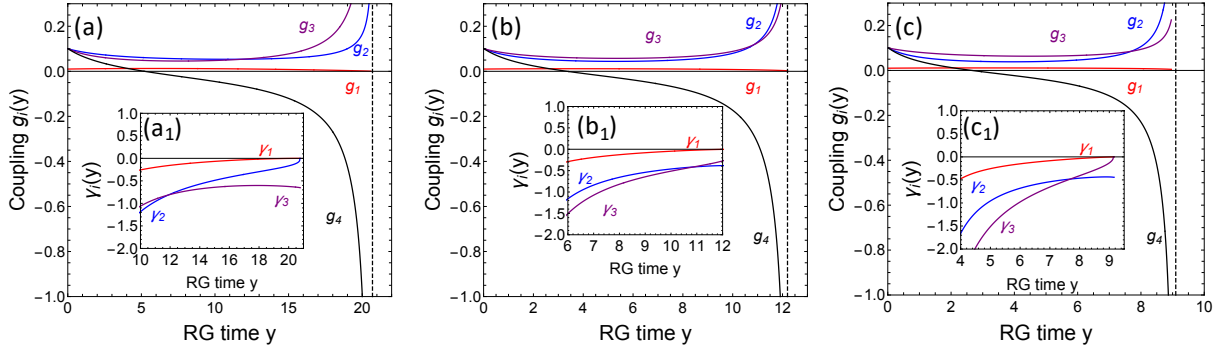


FIG. 5. RG flows of couplings $g_i(y)$ and reduce parameters $\gamma_i(y)$ with initial condition $g_1(0) = 0.01$ and $g_2(0) = g_3(0) = g_4(0) = 0.1$ for the hexagonal lattice $N_p = 3$. Here the nesting parameter is taken as $d_0 = 0.5$. (a),(b),(c) shows the RG flows of the couplings with RG time y for fermion flavors $N_f = 2, 4$ and 6 , respectively. The black dashed line denote the critical RG time y_c where some coupling strength diverge. The inset display the RG flows of $\gamma_i(y)$ near critical RG time y_c . ($\gamma_1(y), \gamma_2(y), \gamma_3(y)$) tend to flow to a stable fixed point at a given initial parameters for the reduced RG equations (14)-(16).

and their stability from the 3D RG flow diagram through numerical calculations. For example, we plot such a diagram in Fig. 4 for the case of hexagonal lattice with $N_p = 3$ and $N_f = 4$ (two fold VHSs), where the initial interactions are $g_4(y=0) = -0.1$ and the nesting parameter is $d_0 = 0.1$. From Fig. 4, it is apparent that the unstable fixed points denoted by black points will flow to one of the fixed points denoted by red point with a small perturbation. The relative interactions ($\Gamma_1, \Gamma_2, \Gamma_3$) of two stable points, labeled by A and B, are $(0, 0, -0.466)$ and $(0, 0, 0.966)$, respectively. The corresponding interactions (G_1, G_2, G_3, G_4) are $(0, 0, 0.304, -0.652)$ and $(0, 0, -0.326, -0.377)$, respectively. Therefore, from the coefficients λ of the competing orders listed in the Table I, we find that the dominant instabilities at the fixed points A and B are d - and s -wave superconducting states, respectively.

VII. PHASE TRANSITION DRIVEN BY THE NUMBER OF FLAVORS

For conventional VHSs, the leading instabilities significantly depend on the number of patches (type of lattice), even for the same initial interaction setting. For example, with initial repulsive interactions, the RG analysis reveals that the d -wave superconducting state and spin density wave (SDW) state are competing on the square lattice⁴, while the chiral d -wave superconducting states become the dominant on the hexagonal lattice⁶. The number of flavor also has a dramatic effect on the competing states even at conventional van Hove filling⁴⁹. In this section, we explore the effect of number of flavors and lattice type competing states for higher-order VHSs through the RG analysis. Driven by the recent progresses in the experimental and theoretical studies in the Kagome material AV_3Sb_5 with the hexagonal structure¹⁶⁻²¹, we first solve the RG equations (9)-(12) for the hexagonal lattice with patches $N_p = 3$ and different N_f (the different orbital

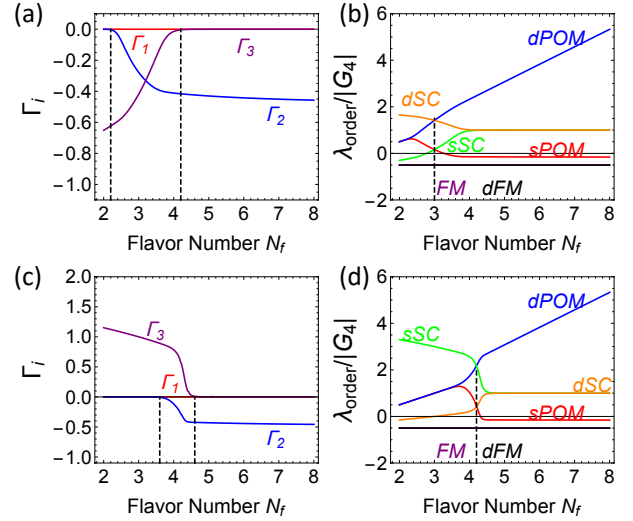


FIG. 6. On the hexagonal lattice with $N_p = 3$, the solution $\Gamma_i = G_i/G_4$ and the ratio of susceptibility coefficient λ and $|G_4|$ for different competing orders as functions of fermion flavors N_f with fixed nesting parameter $d_0 = 0.5$. The two black dashed lines separate three regions $(0, 0, G_3, G_4)$, $(0, G_2, G_3, G_4)$ and $(0, G_2, 0, G_4)$ for the curves for Γ_i . And the dashed black line in curves $\lambda_{\text{order}}/|G_4|$ denotes the position where the phase transition occurs. (a) and (b) are solutions for initial coupling constants $g_{2,3,4}(0) = 0.1$ and $g_1(0) = 0.01$. (c) and (d) are solutions for $g_{2,4}(0) = 0.1$, $g_1(0) = 0.01$ and $g_3(0) = -0.1$.

degeneracies). As shown in Fig. 5, we plot the representative RG flows of coupling strength $g_i(y)$ and reduced parameters $\gamma_i(y)$ (insets) under the RG time y with initial repulsive interactions $g_2(0) = g_3(0) = g_4(0) = 0.1$ and $g_1(0) = 0.01$, and a reasonable nesting parameter $d_0 = 0.5$. The three plots are for the number of flavors $N_f = 2, 4$ and 6 , respectively. For the repulsive coupling strength region $g_i(0) = g_0$ ($i = 2, 3, 4$) and $g_1(0) \ll g_0$, $g_1(y)$ always tends to vanish, while

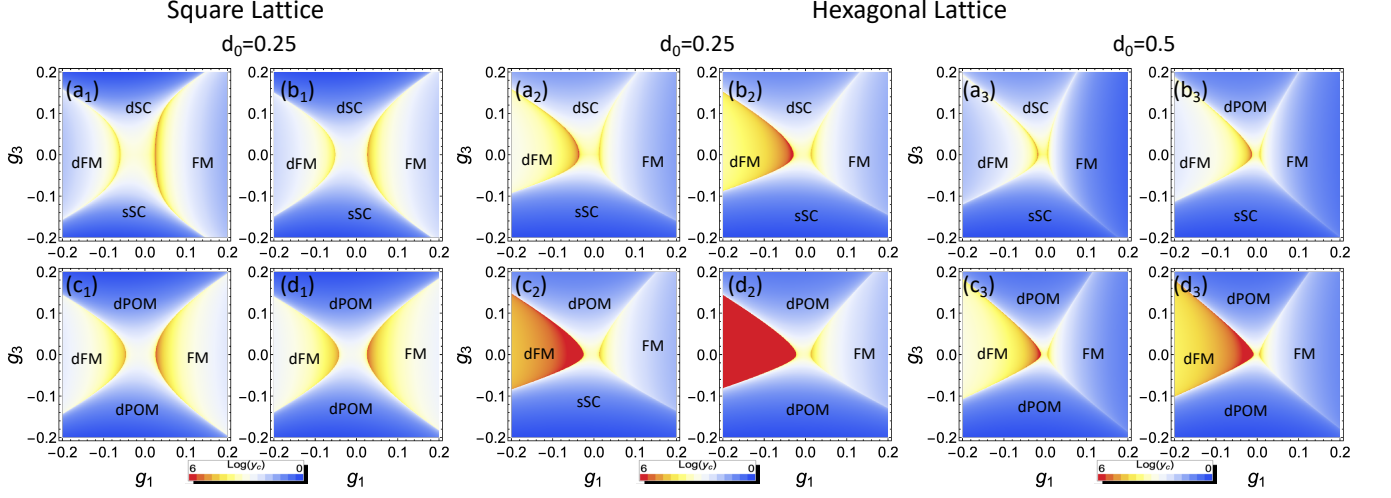


FIG. 7. The phase diagrams for the square and hexagonal lattices in the weak coupling space $(g_1(0), g_3(0))$ with fixed initial repulsive intra- and inter-patch forward coupling strength $g_2(0) = g_4(0) = 0.1$. Here subgraphs $(a_{1,2,3})$, $(b_{1,2,3})$, $(c_{1,2,3})$ and $(d_{1,2,3})$ represent different fermion flavors $N_f = 2, 4, 6$ and 8 , respectively. The left four panels display the case of the square lattice with $N_p = 2$ and $d_0 = 0.25$, while the right eight panels show the case of the hexagonal lattices with $N_p = 3$ and $d_0 = 0.25$ and $d_0 = 0.5$. In all panels there are four different phases, which are either superconducting (SC), ferromagnetic (FM), or Pomeranchuk (POM) with s-wave (s) or d-wave (d) form factor. The color in the phase diagrams encodes the information of critical RG time y_c as $\ln(y_c)$.

$g_4(y)$ eventually changes sign and diverges to negative infinity. Thus, in this region, the negative G_4 will favor the charge Pomeranchuk and superconducting states. The detailed numerical results shown in Fig. 5 indicate that $g_2(y)$ and $g_3(y)$ flow to positive infinite, while it is subtle to tell which one diverges first. For the normal case with $N_f = 2$, Fig. 5 (a) and (a₁) show that $g_3(y)$ behaves as $g_3(y) \sim 1/(y_c - y)$, i.e., with a similar power-law divergence as $g_4(y)$, while $g_2(y)$ has a much slower power-law divergence $1/(y_c - y)^\alpha$ with the exponent $0 < \alpha \approx -2d_0(N_f - 1)G_4 < 1$. In this case, the fixed trajectory is $(0, 0, G_3, G_4)$ with $G_3 > 0$ and $G_4 < 0$. For the case with $N_f = 4$ (from the orbital degeneracy), the flow of interactions are depicted in Fig. 5 (b) and (b₁), both $g_2(y)$ and $g_3(y)$ will diverge as $g_{2/3}(y) \sim 1/(y_c - y)$. As a consequence, the fixed trajectory for this case is $(0, G_2, G_3, G_4)$ with $G_2, G_3 > 0$ and $G_4 < 0$. For the case with $N_f = 6$, as shown in Fig. 5 (c) and (c₁), $g_2(y)$ and $g_3(y)$ have a reversed behavior compared to the case of $N_f = 2$, $g_2(y)$ scales as $1/(y_c - y)$, but $g_3(y)$ behaves slower as $1/(y_c - y)^\alpha$ with $0 < \alpha' \approx -2G_4 < 1$. Here the fixed trajectory is $(0, G_2, 0, G_4)$ with $G_2 > 0$ and $G_4 < 0$.

To clearly demonstrate the evolution of relative interactions, we plot Γ_i as function of the number of flavors N_f in Fig. 6 (a). $|\Gamma_2|$ becomes nonzero from $N_f = 2.2$ and increases with increasing N_f . In contrast, $|\Gamma_3|$ decreases with increasing N_f and drops to zero at $N_f = 4.2$. These behaviors are intimately related to the RG equations. From the Eq. (12), we find that g_4 diverges faster and the critical y_c becomes smaller with increasing N_f , which is already numerically verified in Fig. 5. The more divergent negative g_4 and increasing N_f have a positive

feedback for the g_2 from the Eq. (10), significantly enhancing g_2 . While, as the one-loop correction of g_3 is decoupled from g_2 and does not depend on N_f , g_3 is slightly enhanced. The reduction of critical RG time y_c with increasing N_f will lead to a decreasing Γ_3 . The relative evolution of G_2 and G_3 in the regions $g_0 > 0$ and $g_0 \gg g_1(0) > 0$ with increasing flavor number N_f for the hexagonal lattice will generate a phase transition from a particle-particle instability to a particle-hole instability. Here, with increasing N_f , λ_{dSC} decreases but λ_{dPOM} increases monotonically, as shown in Fig. 6 (b), and thus the phase transition is from the d-wave superconducting state to the d-wave Pomeranchuk state. The phase transition occurs around $N_f = 3$. With an initial attractive g_3 , the behaviors are similar to the case of repulsive g_3 as shown in Fig. 6 (c), where $|\Gamma_2|$ increases and $|\Gamma_3|$ decreases with increasing N_f . The difference is that the phase transition is from the s-wave superconducting state to the d-wave Pomeranchuk state and occurs at a larger $N_f = 4.2$ as illustrated in Fig. 6 (d).

We further study the phase diagrams of competing states in a wider range of initial interactions on the square and hexagonal lattice. In Fig. 7, we take the initial intra- and inter-patch forward coupling strength as repulsive with $g_4(0) = g_2(0) = 0.1$ and plot the diagrams in the coupling space $(g_1(0), g_3(0))$ for the square and hexagonal lattices. The small subplots $(a_{1,2,3})$, $(b_{1,2,3})$, $(c_{1,2,3})$ and $(d_{1,2,3})$ are calculated with the number of fermion flavors being $N_f = 2, 4, 6$ and 8 , respectively. The two lattice structures share very similar phase diagrams for the same initial parameters, distinct from the case of conventional VHSs. Furthermore, one can ob-

serve that phase diagrams are separated into four regions. The ferromagnetic and anti-ferromagnetic (d-wave ferromagnetic) orders are robust in a wide range of coupling space for different nesting parameter d_0 and fermion flavors. For large initial negative and positive g_3 , the system with small N_f favors an s-wave and d-wave superconducting state, respectively. With the gradual increase of N_f , these orders turn to be the dPOM state. The transition from superconducting states to dPOM occurs at smaller N_f with a larger nesting parameter d_0 , as shown in phase diagrams (Fig. 7 (b₂) and (b₃)) of the hexagonal lattice with $d_0 = 0.25$ and $d_0 = 0.5$. In the square lattice with $N_p = 2$, the phase diagrams with $d_0 = 0.5$ are similar to the case with $d_0 = 0.25$ and they are displayed in the Appendix C. A supermetal phase, exhibiting power-law divergent DOS but no long-range order¹², can appear on the hexagonal lattice at $d_0 = 0.25$ and $N_f = 8$ (red regime of the sub-figure (d₂) of Fig. 7). The phase diagrams with a variation of other couplings $g_2(0)$ and $g_4(0)$ are provided in the appendix D. They also display a similar feature that the instabilities in the particle-particle channel are suppressed but particle-hole orders are favored with increasing flavor number N_f .

VIII. DISCUSSION

We discuss the ground state for the dominant states with degeneracy. On the square lattice, there are two saddle points and $N_p = 2$. All competing states are non-degenerate, consistent with lattice symmetry. In the hexagonal lattice, such as, honeycomb or kagome lattices, there are three saddle points and $N_p = 3$. There is a single s-wave state and two-fold degenerate d-wave states in each channel of instability, including superconductivity, spin density wave and charge density wave, with zero momentum transfer (Pomeranchuk order). In the following, we take the kagome lattice as an example. In the superconducting channel, for the d-wave pairing state, the system tends to form a $d + id$ state^{6,14} in order to maximize the condensation energy. This state is time-reversal breaking and carries an even Chern number. In the channel of spin density wave, the s-wave state is the ferromagnetic state and the magnetic moments of the three patches are aligned along the same direction, as shown in Fig. 8 (a). The d-wave states are two-fold degenerate and the corresponding eigenvectors are $\phi_1^d = \frac{1}{\sqrt{6}}(1, 1, -2)$ and $\phi_2^d = \frac{1}{\sqrt{2}}(1, -1, 0)$. The order parameter can be written as $\mathbf{S}_d = \mathbf{s}_1\phi_1^d + \mathbf{s}_2\phi_2^d$ and the corresponding free energy up to quartic order in $\mathbf{s}_{1,2}$ reads¹⁴,

$$F_d^M = \frac{\alpha}{2}(\mathbf{s}_1^2 + \mathbf{s}_2^2) + \frac{\beta}{2}[(\mathbf{s}_1^2 + \mathbf{s}_2^2)^2 - \frac{4}{3}\mathbf{s}_1^2\mathbf{s}_2^2 + \frac{4}{3}(\mathbf{s}_1 \cdot \mathbf{s}_2)^2]. \quad (17)$$

As β is generally greater than zero, by minimizing the free energy, we obtain that \mathbf{s}_1 and \mathbf{s}_2 are orthogonal with the same amplitude. Setting these two vectors to be the

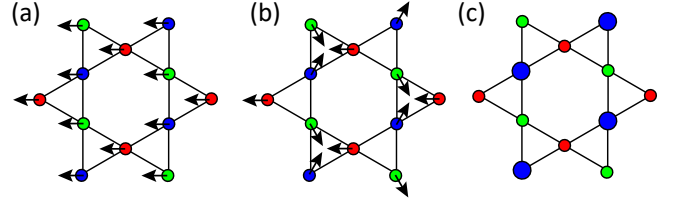


FIG. 8. Competing states in the kagome lattice: (a) ferromagnetic order, (b) 120° antiferromagnetic order (c) nematic order. The size of a circle represents the onsite energy of the corresponding sublattice.

in-plane unit vectors \mathbf{e}_x and \mathbf{e}_y , the corresponding order parameter is $\mathbf{S}_d = \frac{1}{\sqrt{6}}(\mathbf{e}_x + \sqrt{3}\mathbf{e}_y, \mathbf{e}_x - \sqrt{3}\mathbf{e}_y, -2\mathbf{e}_x)$. In the momentum space, the spin vector winds twice on the Fermi surface. For the p-type VHS in the kagome lattice, where each sublattice dominates the eigen state at each saddle point, this order corresponds to the intra-unit-cell antiferromagnetic order with an angle of 120° between nearby spins, as shown in Fig. 8 (b). For the m-type VHS, where the eigenstate at each saddle point is attributed to a mixture of two sublattices, this order corresponds to both onsite and bond orders and thus there is no clear real-space pattern. In the channel of charge density wave, the s-wave state is isotropic and preserve all lattice symmetry. While, the d-wave states are two-fold degenerate and the eigen vectors are the same as the d-wave spin density wave state. The order parameter can be written as $\eta_d^C = \eta_1\phi_1^d + \eta_2\phi_2^d$. The free energy reads^{14,54–56},

$$F_d^C = \frac{\alpha'}{2}(\eta_1^2 + \eta_2^2) + \frac{\beta'}{2}(\eta_-^3 + \eta_+^3), \quad (18)$$

where $\eta_{\pm} = \eta_1 \pm i\eta_2$ and the cubic term is attributed to the six-fold rotation of the lattice. Assuming $\eta_{\pm} = \eta e^{\pm 2i\theta}$ with θ being the orientation of the nematic director, the cubic term can be written as $\beta'\eta^3\cos(6\theta)$, which is minimized by $2\theta = 2n\pi/3$ for $\beta' < 0$ and $2\theta = (2n+1)\pi/3$ for $\beta' > 0$. The corresponding order parameters are $\eta_d^C = \frac{1}{\sqrt{6}}(2, -1, -1)$, $\frac{1}{\sqrt{6}}(-1, 2, -1)$ or $\frac{1}{\sqrt{6}}(-1, -1, 2)$. These orders break the lattice rotational symmetry and thus are nematic. For the p-type VHS, this order corresponds to distinct onsite energies of sublattices (see Fig. 8 (c)) or anisotropic intrasublattice hopping. For the m-type VHS, sublattices are mixed and this order is attributed to distinct onsite energies of sublattice and anisotropic intra- and inter-sublattice hopping.

Let us now discuss the implications of our findings for the kagome metals AV_3Sb_5 . In AV_3Sb_5 , both conventional and higher-order VHSs appear near the Fermi level^{20,21}. The CDW order may originate from the electronic correlation effect enhanced by conventional VHSs^{28–31} or phonon softening²⁷. According to ARPES measurements, the momentum-dependent CDW-induced gaps are maximum at the M point and the conventional VHSs are shifted away from the Fermi level^{20,26,57}. In contrast, the higher-order VHS only exhibits slight en-

ergy shifting²⁶ due to its poor Fermi surface nesting and is still close to the Fermi level in the CDW phase. Superconductivity and nematicity emerging inside the CDW order can derive from the instabilities of this higher-order VHS. The two-fold dPOM states will mix and form a nematic state breaking the lattice rotational symmetry (see Fig. 8 (c)), which may account for the observed nematic order in transport measurements³⁹ and STM measurements³⁷. The superconductivity in experiments is d -wave or s -wave depending on the initial value of the interaction g_3 according to our calculations. With increasing pressure, the CDW and nematic orders get suppressed while superconductivity is enhanced as the both conventional and higher-order VHSs gradually move away from the Fermi level^{58,59}. These are consistent with experimental observations.

IX. CONCLUSIONS AND REMARKS

In summary, we systematically study the competing instabilities on the 2D square and hexagonal lattices at higher-order van Hove filling with an $SU(N_f)$ flavor degeneracy. These higher-order VHSs host the power-law divergent DOS and feature poor Fermi surface nesting. Firstly, we study the evolution of the band structure and explore the realization of higher-order VHSs on square and kagome lattices, based on tight-binding Hamiltonian and effective model around saddle points. Secondly, by performing renormalization group calculations, we investigate the competing orders with a variation of initial coupling constants and number of fermion flavors. Interestingly, we find that increasing flavor number can drive a generic phase transition from a superconductivity order to a nematic order. It originates from the significant enhancement of the inter patch density interaction g_2 with a larger flavor number N_f . Thirdly, the mean-field theory is used to determine the ground states and their real space patterns are also revealed on the kagome lattices. Implications for observed intriguing states in AV_3Sb_5 kagome metals are also discussed.

X. ACKNOWLEDGMENTS

X. L. Han acknowledges supports from China Postdoctoral Science Foundation Fellowship (No. 2022M723112).

Appendix A: Fixed trajectories and their stabilities on the square lattice

In this section, we can get the equations for the fixed trajectories by putting the relation $g_i(y) = G_i/(y_c - y)$

near critical time y_c into Eq. (9)-(12) as following,

$$G_1 = 2d_0G_1G_4, \quad (A1)$$

$$G_3 = -2G_3G_4, \quad (A2)$$

$$G_2 = -2d_0G_4((N_f - 1)G_2 - G_1), \quad (A3)$$

$$G_4 = -G_4^2 - G_3^2 - d_0N_fG_2^2 - 2d_0G_1G_2 - d_0G_1^2 - d_0G_4^2, \quad (A4)$$

for the square lattice case with $N_p = 2$. The fixed trajectories can be analyzed by using the stability matrix mentioned in the section. VI. We summarize the solutions and their stability conditions in the table. A.

Appendix B: Fixed trajectories on the hexagonal lattice

The equations of fixed trajectories on the hexagonal lattice with $N_p = 3$ are given as,

$$G_1 = d_0G_1(2G_4 + G_1), \quad (B1)$$

$$G_2 = -d_0G_2(N_fG_2 - 2G_1) - 2d_0G_4((N_f - 1)G_2 - G_1), \quad (B2)$$

$$G_3 = -G_3(G_3 + 2G_4), \quad (B3)$$

$$G_4 = -d_0(2N_fG_2^2 - 4G_1G_2 - 2G_1^2 + (N_f - 3)G_4^2) - G_4^2 - 2G_3^2. \quad (B4)$$

We solve these equations, and we list these solutions as below.

i: when $G_1 = G_3 = 0$. G_2 and G_4 are given

$$(1) \quad G_2 = 0, G_4 = \frac{-1}{1 + d_0(N_f - 3)}, \quad (B5)$$

$$(2) \quad G_4 = \frac{8d_0 - 9N_f d_0 \pm S_2}{2(N_f d_0 + 8d_0^2 - 19N_f d_0^2 + 9N_f^2 d_0^2)},$$

$$G_2 = \frac{-N_f + 2N_f d_0 \mp (N_f - 1)S_2}{N_f d_0 [N_f + d_0(8 - 19N_f + 9N_f^2)]}, \quad (B6)$$

ii: at the relation $G_1 = \frac{1}{d_0} - 2G_4$, $G_3 = 0$, we solve as

$$(3) \quad G_2 = -2G_4 = \frac{17d_0 \pm S_3}{d_0 - 27d_0^2 + 9N_f d_0^2}, \quad (B7)$$

$$(4) \quad G_2 = \frac{N_f - 2N_f d_0 + N_f^2 d_0 \pm S_4}{N_f(N_f - 8d_0 - 11N_f d_0 + N_f^2 d_0)},$$

$$G_4 = \frac{-8d_0 - 9N_f d_0 \mp S_4}{2(N_f d_0 - 8d_0^2 - 11N_f d_0^2 + N_f^2 d_0^2)}, \quad (B8)$$

iii: when $G_1 = G_2 = 0$ and $G_3 = -1 - 2G_4$, we have,

$$(5) \quad G_4 = -\frac{9 \pm S_5}{2(9 - 3d_0 + N_f d_0)}, \quad (B9)$$

TABLE II. Fixed trajectories and stable conditions on the square lattice

No.	G_1	G_2	G_3	G_4	conditions for fixed trajectories	leading order	stable condition
1	0	0	0	$\frac{-1}{d_0(N_f-3)+1}$	$N_f \neq 3 - \frac{1}{d_0}$	sPom/dPom	unstable
2	0	$\sqrt{\frac{d_0 N_f + d_0 - 1}{4d_0^3 N_f (N_f - 1)^2}}$	0	$\frac{-1}{2d_0(N_f - 1)}$	$N_f \geq \frac{1}{d_0} - 1$	dPom	$N_f \geq 1 + \frac{1}{d_0}$
3	0	$-\sqrt{\frac{d_0 N_f + d_0 - 1}{4d_0^3 N_f (N_f - 1)^2}}$	0	$\frac{-1}{2d_0(N_f - 1)}$	$N_f \geq \frac{1}{d_0} - 1$	sPom	$N_f \geq 1 + \frac{1}{d_0}$
4	0	0	$\frac{\sqrt{1-d_0(N_f-3)}}{2}$	$-\frac{1}{2}$	$N_f \leq \frac{1}{d_0} + 3$	dSC or sPom/dPom	$N_f \leq 3 + \frac{1}{d_0}$
5	0	0	$-\frac{\sqrt{1-d_0(N_f-3)}}{2}$	$-\frac{1}{2}$	$N_f \leq \frac{1}{d_0} + 3$	sSC	$N_f \leq 1 + \frac{1}{d_0}$
6	$N_f G_2$	$\sqrt{\frac{1+d_0(N_f-1)}{4d_0^3(N_f+N_f^2)}}$	0	$\frac{1}{2d_0}$	$N_f \geq 1$	FM	$N_f \geq 1$
7	$N_f G_2$	$-\sqrt{\frac{1+d_0(N_f-1)}{4d_0^3(N_f+N_f^2)}}$	0	$\frac{1}{2d_0}$	$N_f \geq 1$	dFM	$N_f \geq 1$

iv: when $G_1 = 0$ and $G_3 = -1 - 2G_4$, we can solve,

$$(6) \quad G_4 = \frac{8d_0 - 17N_f d_0 \mp S_6}{2(9N_f d_0 + 8d_0^2 - 19N_f d_0^2 + 9N_f^2 d_0^2)},$$

$$G_2 = \frac{-9N_f d_0 - 6N_f d_0^2 + 8N_f^2 d_0^2 \pm d_0(N_f - 1)S_6}{9N_f d_0 + 8d_0^2 - 19N_f d_0^2 + 9N_f^2 d_0^2}, \quad (B10)$$

v: when $G_1 = \frac{1}{d_0} - 2G_4$ and $G_3 = -1 - 2G_4$, we can solve,

$$(7) \quad G_2 = \frac{25d_0 \pm S_7}{9(d_0 - 3d_0^2 + N_f d_0^2)},$$

$$G_4 = \frac{-25d_0 \mp S_7}{18(d_0 - 3d_0^2 + N_f d_0^2)}, \quad (B11)$$

$$(8) \quad G_2 = \frac{9N_f d_0 + 6N_f d_0^2 + N_f^2 d_0^2 \pm d_0 S_8}{N_f d_0(9N_f d_0 - 8d_0^2 - 11N_f d_0^2 + N_f^2 d_0^2)},$$

$$G_4 = \frac{-8d_0 - 17N_f d_0 \mp S_8}{2(9N_f d_0 - 8d_0^2 - 11N_f d_0^2 + N_f^2 d_0^2)}, \quad (B12)$$

here we define the following formulas as,

$$S_2 = \sqrt{N_f d_0(-8 + 8d_0 + 9N_f d_0)}, \quad (B13)$$

$$S_3 = \sqrt{d_0(8 + 73d_0 + 72N_f d_0)}, \quad (B14)$$

$$S_4 = \sqrt{N_f d_0(8 + 8N_f - 8d_0 + N_f d_0 + 8N_f^2 d_0)}, \quad (B15)$$

$$S_5 = \sqrt{9 + 24d_0 - 8N_f d_0}, \quad (B16)$$

$$S_6 = (-72N_f d_0 - 120N_f d_0^2 + 145N_f^2 d_0^2 - 64N_f d_0^3 + 152N_f^2 d_0^3 - 72N_f^3 d_0^3)^{1/2} \quad (B17)$$

$$S_7 = \sqrt{d_0(72 + 337d_0 + 72N_f d_0 + 216d_0^2 - 72N_f d_0^2)}, \quad (B18)$$

$$S_8 = \left[(8d_0 + 17N_f d_0)^2 - 4(-2 - 2N_f + 2N_f d_0) \times (9N_f d_0 - 8d_0^2 - 11N_f d_0^2 + N_f^2 d_0^2) \right]^{1/2}. \quad (B19)$$

One can note the solutions of fixed trajectories on the hexagonal lattice are too complex to analysis their stable properties, in contrast to the case on the square lattice.

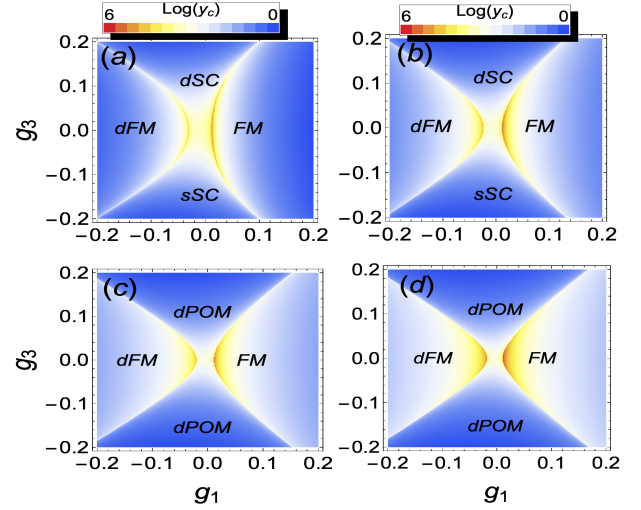


FIG. 9. The phase diagrams for the square lattice in the weak coupling space ($g_1(0), g_3(0)$) with fixed initial repulsive intra- and inter-patch forward coupling strength $g_2(0) = g_4(0) = 0.1$, and with the given nesting parameter $d_0 = 0.5$. Here (a-d) is for the case with $N_f = 2, 4, 6$ and 8 , respectively.

Appendix C: Phase diagrams for the square lattice with the large nesting parameter

The phase diagram with the nesting parameter $d_0 = 0.5$ in the square lattice is given in Fig. 9. It is clear to see there is no dramatic difference comparing $d_0 = 0.25$ and $d_0 = 0.5$ in the given initial coupling constant ($g_2(0), g_4(0)$) = (0.1, 0.1).

Appendix D: Phase diagrams for the negative initial coupling constant

We plot the phase diagrams with the nesting parameter $d_0 = 0.5$ in the hexagonal and square lattice for the dif-

ferent given initial coupling constant ($g_2(0), g_4(0)$). From the Fig. 10, one can note that there exist phase transition from superconductivity to the s - or d -wave charge order (sPOM or dPOM) as increasing the fermion flavor N_f .

-
- * hanxinloong@gmail.com
† a.schnyder@fkf.mpg.de
‡ xxwu@itp.ac.cn
- ¹ H. J. Schulz, *Europhysics Letters* **4**, 609 (1987).
 - ² Dzyaloshinskii, *JETP Lett* **46** (1987).
 - ³ N. Furukawa, T. M. Rice, and M. Salmhofer, *Phys. Rev. Lett.* **81**, 3195 (1998).
 - ⁴ K. L. Hur and T. Maurice Rice, *Annals of Physics* **324**, 1452 (2009).
 - ⁵ L. Van Hove, *Phys. Rev.* **89**, 1189 (1953).
 - ⁶ R. Nandkishore, L. S. Levitov, and A. V. Chubukov, *Nature Physics* **8**, 158 (2012).
 - ⁷ M. L. Kiesel, C. Platt, W. Hanke, D. A. Abanin, and R. Thomale, *Phys. Rev. B* **86**, 020507 (2012).
 - ⁸ W.-S. Wang, Y.-Y. Xiang, Q.-H. Wang, F. Wang, F. Yang, and D.-H. Lee, *Phys. Rev. B* **85**, 035414 (2012).
 - ⁹ A. M. Black-Schaffer and C. Honerkamp, *Journal of Physics: Condensed Matter* **26**, 423201 (2014).
 - ¹⁰ A. Shtyk, G. Goldstein, and C. Chamon, *Phys. Rev. B* **95**, 035137 (2017).
 - ¹¹ N. F. Yuan, H. Isobe, and L. Fu, *Nature communications* **10**, 5769 (2019).
 - ¹² H. Isobe and L. Fu, *Phys. Rev. Res.* **1**, 033206 (2019).
 - ¹³ D. Guerci, P. Simon, and C. Mora, *Phys. Rev. Res.* **4**, L012013 (2022).
 - ¹⁴ L. Classen, A. V. Chubukov, C. Honerkamp, and M. M. Scherer, *Phys. Rev. B* **102**, 125141 (2020).
 - ¹⁵ Y.-P. Lin and R. M. Nandkishore, *Phys. Rev. B* **102**, 245122 (2020).
 - ¹⁶ B. R. Ortiz, L. C. Gomes, J. R. Morey, M. Winiarski, M. Bordelon, J. S. Mangum, I. W. H. Oswald, J. A. Rodriguez-Rivera, J. R. Neilson, S. D. Wilson, E. Ertekin, T. M. McQueen, and E. S. Toberer, *Phys. Rev. Mater.* **3**, 094407 (2019).
 - ¹⁷ B. R. Ortiz, S. M. L. Teicher, Y. Hu, J. L. Zuo, P. M. Sarte, E. C. Schueller, A. M. M. Abeykoon, M. J. Krogstad, S. Rosenkranz, R. Osborn, R. Seshadri, L. Balents, J. He, and S. D. Wilson, *Phys. Rev. Lett.* **125**, 247002 (2020).
 - ¹⁸ T. Neupert, M. M. Denner, J.-X. Yin, R. Thomale, and M. Z. Hasan, *Nature Physics* **18**, 137 (2022).
 - ¹⁹ K. Jiang, T. Wu, J.-X. Yin, Z. Wang, M. Z. Hasan, S. D. Wilson, X. Chen, and J. Hu, *National Science Review* **10**, nwac199 (2023).
 - ²⁰ M. Kang, S. Fang, J.-K. Kim, B. R. Ortiz, S. H. Ryu, J. Kim, J. Yoo, G. Sangiovanni, D. Di Sante, B.-G. Park, *et al.*, *Nature Physics* **18**, 301 (2022).
 - ²¹ Y. Hu, X. Wu, B. R. Ortiz, S. Ju, X. Han, J. Ma, N. C. Plumb, M. Radovic, R. Thomale, S. D. Wilson, *et al.*, *Nature Communications* **13**, 2220 (2022).
 - ²² Y.-X. Jiang, J.-X. Yin, M. M. Denner, N. Shumiya, B. R. Ortiz, G. Xu, Z. Guguchia, J. He, M. S. Hossain, X. Liu, *et al.*, *Nature materials* **20**, 1353 (2021).
 - ²³ Z. Liang, X. Hou, F. Zhang, W. Ma, P. Wu, Z. Zhang, F. Yu, J.-J. Ying, K. Jiang, L. Shan, Z. Wang, and X.-H. Chen, *Phys. Rev. X* **11**, 031026 (2021).
 - ²⁴ C. Li, X. Wu, H. Liu, C. Polley, Q. Guo, Y. Wang, X. Han, M. Dendzik, M. H. Berntsen, B. Thiagarajan, Y. Shi, A. P. Schnyder, and O. Tjernberg, *Phys. Rev. Res.* **4**, 033072 (2022).
 - ²⁵ M. Kang, S. Fang, J. Yoo, B. R. Ortiz, Y. M. Oey, J. Choi, S. H. Ryu, J. Kim, C. Jozwiak, A. Bostwick, *et al.*, *Nature Materials* **22**, 186 (2023).
 - ²⁶ Y. Hu, X. Wu, B. R. Ortiz, X. Han, N. C. Plumb, S. D. Wilson, A. P. Schnyder, and M. Shi, *Phys. Rev. B* **106**, L241106 (2022).
 - ²⁷ H. Tan, Y. Liu, Z. Wang, and B. Yan, *Phys. Rev. Lett.* **127**, 046401 (2021).
 - ²⁸ X. Feng, K. Jiang, Z. Wang, and J. Hu, *Science bulletin* **66**, 1384 (2021).
 - ²⁹ M. M. Denner, R. Thomale, and T. Neupert, *Phys. Rev. Lett.* **127**, 217601 (2021).
 - ³⁰ Y.-P. Lin and R. M. Nandkishore, *Phys. Rev. B* **104**, 045122 (2021).
 - ³¹ T. Park, M. Ye, and L. Balents, *Phys. Rev. B* **104**, 035142 (2021).
 - ³² C. Zhao, L. Wang, W. Xia, Q. Yin, J. Ni, Y. Huang, C. Tu, Z. Tao, Z. Tu, C. Gong, *et al.*, *arXiv preprint arXiv:2102.08356* (2021).
 - ³³ Y. Wang, S. Yang, P. K. Sivakumar, B. R. Ortiz, S. M. Teicher, H. Wu, A. K. Srivastava, C. Garg, D. Liu, S. S. Parkin, *et al.*, *arXiv preprint arXiv:2012.05898* (2020).
 - ³⁴ H. Li, H. Zhao, B. R. Ortiz, T. Park, M. Ye, L. Balents, Z. Wang, S. D. Wilson, and I. Zeljkovic, *Nature Physics* **18**, 265 (2022).
 - ³⁵ X. Wu, T. Schwemmer, T. Müller, A. Consiglio, G. Sangiovanni, D. Di Sante, Y. Iqbal, W. Hanke, A. P. Schnyder, M. M. Denner, M. H. Fischer, T. Neupert, and R. Thomale, *Phys. Rev. Lett.* **127**, 177001 (2021).
 - ³⁶ H. Zhao, H. Li, B. R. Ortiz, S. M. Teicher, T. Park, M. Ye, Z. Wang, L. Balents, S. D. Wilson, and I. Zeljkovic, *Nature* **599**, 216 (2021).
 - ³⁷ L. Nie, K. Sun, W. Ma, D. Song, L. Zheng, Z. Liang, P. Wu, F. Yu, J. Li, M. Shan, *et al.*, *Nature* **604**, 59 (2022).
 - ³⁸ H. Li, H. Zhao, B. R. Ortiz, T. Park, M. Ye, L. Balents, Z. Wang, S. D. Wilson, and I. Zeljkovic, *Nature Physics* **18**, 265 (2022).
 - ³⁹ Y. Xiang, Q. Li, Y. Li, W. Xie, H. Yang, Z. Wang, Y. Yao, and H.-H. Wen, *Nature communications* **12**, 6727 (2021).
 - ⁴⁰ K. Y. Chen, N. N. Wang, Q. W. Yin, Y. H. Gu, K. Jiang, Z. J. Tu, C. S. Gong, Y. Uwatoko, J. P. Sun, H. C. Lei, J. P. Hu, and J.-G. Cheng, *Phys. Rev. Lett.* **126**, 247001 (2021).
 - ⁴¹ X. Chen, X. Zhan, X. Wang, J. Deng, X.-B. Liu, X. Chen, J.-G. Guo, and X. Chen, *Chinese Physics Letters* **38**, 057402 (2021).
 - ⁴² Z. Zhang, Z. Chen, Y. Zhou, Y. Yuan, S. Wang, J. Wang, H. Yang, C. An, L. Zhang, X. Zhu, Y. Zhou, X. Chen, J. Zhou, and Z. Yang, *Phys. Rev. B* **103**, 224513 (2021).

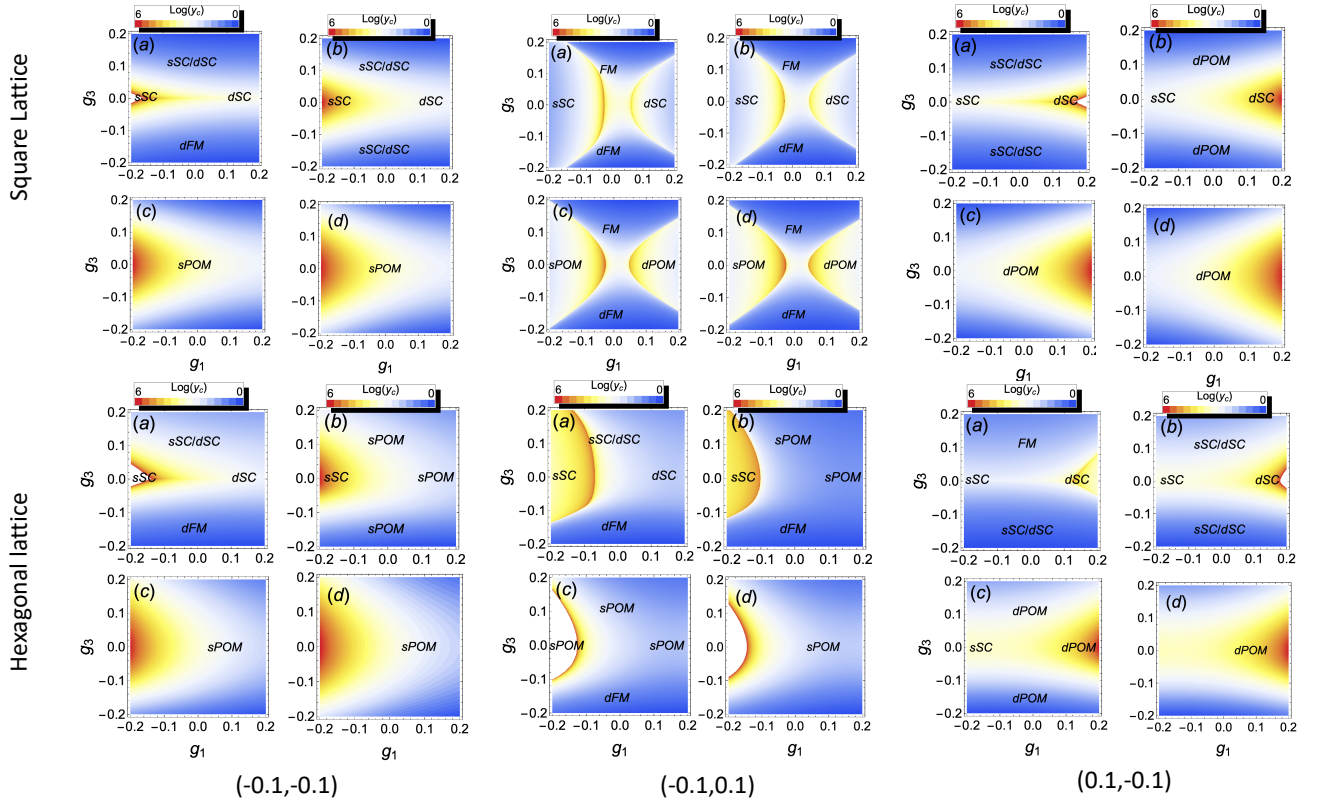


FIG. 10. The phase diagrams for the square and hexagonal lattice in the weak coupling space ($g_1(0), g_3(0)$) with different fixed initial repulsive intra- and inter-patch forward coupling strength ($g_2(0), g_4(0)$), and with the given nesting parameter $d_0 = 0.25$. Here (a-d) is for the case with $N_f = 2, 4, 6$ and 8 respectively. The upper panel is for the square lattice, and down panel is for the hexagonal lattice. The initial given coupling constant ($g_2(0), g_4(0)$) is $(-0.1, -0.1)$ for the left panel, $(-0.1, 0.1)$ for the middle panel, and $(0.1, -0.1)$ for the right panel respectively.

- ⁴³ M. L. Kiesel and R. Thomale, *Phys. Rev. B* **86**, 121105 (2012).
- ⁴⁴ H. D. Scammell, J. Ingham, T. Li, and O. P. Sushkov, *Nature Communications* **14**, 605 (2023).
- ⁴⁵ Y.-M. Wu, R. Thomale, and S. Raghu, *arXiv preprint arXiv:2211.01388* (2022).
- ⁴⁶ D. V. Efremov, A. Shtyk, A. W. Rost, C. Chamon, A. P. Mackenzie, and J. J. Betouras, *Phys. Rev. Lett.* **123**, 207202 (2019).
- ⁴⁷ A. Ramires, P. Coleman, A. H. Nevidomskyy, and A. M. Tsvelik, *Phys. Rev. Lett.* **109**, 176404 (2012).
- ⁴⁸ D. Di Sante, X. Wu, M. Fink, W. Hanke, and R. Thomale, *Phys. Rev. B* **99**, 201106 (2019).
- ⁴⁹ Y.-P. Lin and R. M. Nandkishore, *Phys. Rev. B* **100**, 085136 (2019).
- ⁵⁰ H. Yao and F. Yang, *Phys. Rev. B* **92**, 035132 (2015).
- ⁵¹ W. Metzner, M. Salmhofer, C. Honerkamp, V. Meden, and K. Schönhammer, *Rev. Mod. Phys.* **84**, 299 (2012).
- ⁵² W. Qin, L. Li, and Z. Zhang, *Nature Physics* **15**, 796 (2019).
- ⁵³ I. Herbut, *A modern approach to critical phenomena* (Cambridge University Press, 2007).
- ⁵⁴ M. L. Kiesel, C. Platt, and R. Thomale, *Phys. Rev. Lett.* **110**, 126405 (2013).
- ⁵⁵ M. Hecker and J. Schmalian, *npj Quantum Materials* **3**, 26 (2018).
- ⁵⁶ A. Little, C. Lee, C. John, S. Doyle, E. Maniv, N. L. Nair, W. Chen, D. Rees, J. W. Venderbos, R. M. Fernandes, *et al.*, *Nature materials* **19**, 1062 (2020).
- ⁵⁷ H. Luo, Q. Gao, H. Liu, Y. Gu, D. Wu, C. Yi, J. Jia, S. Wu, X. Luo, Y. Xu, *et al.*, *Nature communications* **13**, 273 (2022).
- ⁵⁸ H. LaBollita and A. S. Botana, *Phys. Rev. B* **104**, 205129 (2021).
- ⁵⁹ A. Consiglio, T. Schwemmer, X. Wu, W. Hanke, T. Neupert, R. Thomale, G. Sangiovanni, and D. Di Sante, *Phys. Rev. B* **105**, 165146 (2022).